Soft Matter

ARTICLE

Evaporation and morphological patterns of bi-dispersed colloidal droplets on hydrophilic and hydrophobic surfaces

R. Iqbal,[a] B. Majhy [a], Amy Q. Shen [b] and A. K. Sen *[a]

Understanding of the formation of different morphological patterns depending on the particle size and surface wettability has great relevance in the separation, mixing and concentration of micron/nano particles and biological entities. We report evaporation and morphological patterns of evaporating bi-dispersed colloidal droplets on hydrophilic and hydrophobic surfaces. To explain the underlying mechanisms of various particle distribution patterns, we propose a phenomenological model that accounts for the drag force, van der Waals and electrostatic interaction forces, and surface tension force acting on the particles. In the case of the hydrophilic surface ($\theta \sim 27°$), there is a competition between the frictional force arising due to the van der Waals ($\sim 10^{-8}\ N$) and electrostatic interaction forces ($\sim 10^{-10}\ N$) and the surface tension force ($\sim 10^{-7}\ N$) that depends on the particle size. Consequently, the smaller particles (0.2 and 1.0 µm in diameter) are found to be pinned and form an outer ring at the contact line whereas the larger particles (3.0 and 6.0 µm in diameter) move inward, either form an inner ring or flocculate depending on the particle size. Interestingly a completely different morphological pattern of the micro/nano particles is observed on a hydrophobic substrate ($\theta \sim 110°$): contact line pinning is no longer observed and particles form a centralized deposition pattern. The order of the magnitude of the surface tension force is higher as compared to the frictional force ($\sim 10^{-8}\ N$) thus the particles are driven radially inward and get accumulated at the center of the droplet. Owing to the mixed mode of evaporation toward the end of evaporation, only a fraction of smaller particles travels radially outward due to the coffee-ring effect. Scanning electron microscopy images reveal that smaller particles are present mostly at the center with a small fraction of smaller particles at the edge of the pattern, whereas larger particles are uniformly distributed throughout.

Introduction

Evaporation of liquids containing non-volatile solute particles are ubiquitous in day-to-day life and important for many technological applications such as inkjet printing[1], coating[2], painting[3], DNA/RNA micro arrays[4–6], self-assembly, surface patterning[7],Transmission electron microscopy (TEM)8 and biosensing[9]. The evaporation of droplets with both pure liquids and colloidal suspensions have been widely studied in literature[10–14]. For a pinned droplet over a hydrophilic substrate, the evaporation flux across the liquid-vapour interface is non-uniform. The evaporation rate near the contact line is higher than that at the droplet centre, thus in order to replenish the enhanced loss at the edge of the droplet, a radially outward flow is developed that drives the particles toward the edge, forming a ring-like pattern called "coffee-ring effect"[15].

In addition to droplets containing single-sized particles (i.e. monodispersed colloidal suspensions), droplets containing two different sizes of particles, herein after referred to as bi-

dispersed colloidal droplets/suspensions, have more practical relevance[16,17] such as in separation of micro/nano particles and biological entities, disposable detection kits, lab-on-a-chip and nanochromatography applications, or concentration of two different types of particles/species or biological entities. Thus, understanding how a mixture of micron and nano sized particles in a droplet behave during evaporation is important from the application point of view. Evaporation of bi-dispersed colloidal droplets has been studied by various researchers in the recent past[16–25]. The behaviour of micron and nano sized particles (5 and 0.5 µm) inside a bi-dispersed colloidal droplet was reported by Jung et al.[25]. By using particle tracking velocimetry (PTV), the micron and nano sized particles are driven radially outward toward the three-phase contact line at the early stage of evaporation. However, at the end of the evaporation, the micron sized particles are driven radially inward toward the centre whereas the nanoparticles remain at the edge and form a ring-like deposition pattern. Pinning and de-pinning of droplets of different volumes containing various sizes of microparticles at different concentrations were extensively investigated by Sangani et al.[19]. It was found that apart from particle size, the pinning and de-pinning phenomena also depend on the droplet radius, particle volume fraction, evaporation rate, and the substrate wettability.

A mechanism of reverse particle motion that repels the coffee-ring effect was revealed when the capillary force prevails over

[a.] Microfluidics Laboratory, Department of Mechanical Engineering, IIT Madras, Chennai, India, 600036.
[b.] Micro/Bio/Nano fluidics Unit, Okinawa Institute of Science and Technology Graduate University, Japan, 904-0412.
* Corresponding author: ashis@iitm.ac.in

the outwardly driven evaporative flow or coffee ring flow[24]. It was observed that, on an identical glass substrate, a pure liquid droplet (of decalin) spreads completely whereas the spreading of a particulated droplet (above a critical linear packing fraction) gets inhibited with self-pinning of the contact line[26]. Monteux and Lequeux[23] reported that, for a droplet containing non-volatile particles, a thin, particle-free liquid film is left at the edge of the droplet during evaporation. The depleted film, which depends on the contact angle and the size of the particles, can be used for sorting particles inside the droplet. Using the coffee-ring phenomenon, a nanochromatographic technique for separation of biological entities (microorganisms, IgG antibodies < 10 nm, proteins E. coli $\sim$ 500 nm, mammalian cells and B-lymphoma cells $\sim$ 5 µm) was accomplished with a resolution of the order of 0.1 µm over a range of particles/entities[17]. Recently, the role of the gravity in the evaporation and separation of particles in sessile and pendent droplets was investigated, in which an excellent separation of 1 and 3 µm particles inside a pendant droplet was achieved [27]. The deposition morphology for a droplet containing different sizes and species of nanoparticles was investigated where the heterogeneity in the deposition morphology was eliminated by using a suitable combination of nanoparticles, as reported by Zhong et al[18]. Chhasatia and Sun[21] studied the interaction of two different sizes of particles inside a picoliter sized droplet over substrates having different wettability (ranging from $0° - 85°$).

The current state of the art suggests that there has been some emphasis on understanding the deposition morphology of bi-dispersed colloidal droplets on hydrophilic substrates for potential applications in particle sorting. However, the kinetics of evaporation of a bi-dispersed colloidal droplet and its subsequent morphological deposition patterns on hydrophobic substrates have not been explored, which has potential applications in the mixing and concentration of different sized particles or biological entities. The aim of the present study is to investigate the kinetics of evaporation and the subsequent morphological pattern of a bi-dispersed colloidal droplet (of two different combinations of particle sizes) over both hydrophilic ($\theta \sim 27°$) and hydrophobic ($\theta \sim 110°$) substrates. The interplay between the relevant forces is considered to illustrate the particle migration phenomena and the resulting patterns in various cases.

Materials & Methods

DI water (resistivity of 18.2 MΩ.cm, Millipore), Polydimethylsiloxane (PDMS, Sylgard 184, Dow Corning Toray, Japan), ethanol (Thermo Fisher, U.S.A.) and isopropyl alcohol (IPA) were used as purchased. Polystyrene micro/nano sized beads of four different sizes, as reported in Table 1, were used in the experiments. The bead sample containing a trace amount of sodium azide (added by manufacturer to prevent the bacterial growth) was washed with DI water twice prior to our

experiments to eliminate the influence of sodium azide on the evaporation kinetics. The sample was centrifuged at 6000 rpm for 2 min, the supernatant was pipetted out and the concentrated micron/nano bead sample at the bottom of the vial was collected. The collected bead sample was again mixed with DI water and the process was repeated. Finally, the washed micro/nano bead sample was diluted with DI water to the desired concentration. Prior to each experiment, the micro/nano bead sample was sonicated for >30 min to overcome or prevent particle aggregation. The surface/zeta potentials of the PDMS substrate and the polystyrene micro/nano particles were measured (Otsuka electronics, Japan) and were found to be -11.55 mV and -58.59 mV, respectively. These values were later used for estimating the electrostatic forces.

Glass and Polydimethylsiloxane (PDMS) were used as the hydrophilic and hydrophobic substrate respectively. The contact angles of the hydrophilic and hydrophobic surfaces were measured to be $27° \pm 1°$ and $110° \pm 1°$ respectively. The substrates were cleaned with IPA and ethanol followed by the drying with compressed N_2 before each experiment. Microscopic glass slides of thickness 1.1 mm (Matsunami, Japan) were used as the supporting substrate to fabricate hydrophobic surfaces. Glass slides were spin coated with PDMS at 2000 rpm for 20 s, followed by drying in an oven at 65°C for 12 h in order to obtain a uniform thin film of PDMS layer over the rigid glass substrate.
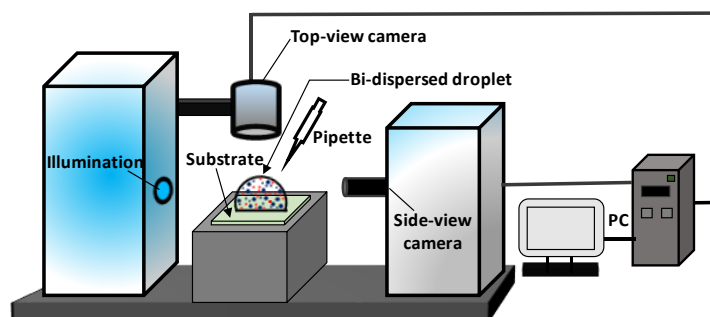
Fig. 1 Schematic of the experimental setup for studying evaporation kinetics of bi-dispersed colloidal droplets.

Table 1 Specifications of polystyrene micro/nano sized beads of four different sizes.

No.	Size (µm)	Colour and vendor	wt%	Fluorescent (Y/N)	Set
1	1.0	Nile red (Thermo Fisher)	2.0	Y (535/575 nm)	A
2	6.0	Yellow (Polysciences)	2.7	N	
3	0.2	Red (Thermo Fisher)	1.0	Y (542/612 nm)	B
4	3.0	Yellow (Polysciences)	2.7	N	

Fig. 1 shows the schematic of the experimental setup. Droplets of 1.0 μL volume were dispensed over different substrates using a micropipette (Gilson, U.S.A.). The evaporation kinetics of the droplets, i.e., contact angle and contact radius were captured using a contact angle meter (Theta Attension, Biolin Scientific, U.S.A.). Once the droplet completely evaporated, the morphological deposition patterns were captured using both a bright-field (Keyence upright microscope, Japan) and a fluorescent microscope (Nikon Eclipse Ti-S, Japan). The morphological deposition patterns were characterized using SEM (FEI Quanta, FEG 250, Japan) and an optical profilometer (Keyence, Japan). Prior to SEM characterization, the substrates were sputter coated (Hitachi, Japan, MCI000, 15 mA, 30 s) with platinum in order to enhance the conductivity for better imaging contrast. The experiments were carried out in a quiescent atmosphere with an ambient temperature of 25° C and relative humidity (RH) of 45 ± 5 % . Each experiment was repeated at least three times in order to ensure repeatability and reproducibility of the data.

Results & Discussions

We first discuss the evaporation kinetics and morphological patterns of bi-dispersed colloidal droplets on hydrophilic substrates, followed by those on a hydrophobic substrate. For both cases, we discuss the potential mechanism on the various pattern formation related to the forces acting on the micro/nano particles during evaporation.

Hydrophilic substrate

The evaporation kinetics and morphological pattern of bi-dispersed colloidal droplets (set A and B in Table 1) over a hydrophilic (glass) substrate are presented in Fig. 2a and 2b. Set A comprises fluorescent particles of size 1.0 μm and non-fluorescent particles of size 6.0 μm, whereas set B comprises a mixture of fluorescent particles of size 0.2 μm and non-fluorescent particles of size 3.0 μm.

Fig. 2a depicts the normalized contact radius ($\hat{r} = r/r_o$) and contact angle (θ) against normalized time ($\hat{t} = t/t_E$) of both sets of bi-dispersed colloidal droplets and a DI water droplet during evaporation with the same droplet volume of 1.0 μL. The instantaneous contact radius is r and the maximum (initial) contact radius of the droplet is r_0. The instantaneous time t is normalized with the total time t_E required for a droplet to evaporate completely. The evaporation time was determined by studying the variation of the contact line radius $r(t)$ with time t. The evaporation time ($t = t_E$) is the time elapsed between the time instant a droplet is dispensed (i.e. $t = 0$) and a time instant where the contact line radius and contact angle reached a steady state (i.e. no further decrease in the contact line radius and contact angle). As observed, in the case of a pure DI water droplet, $\hat{r}$ decreases continuously throughout the evaporation process (after $\hat{t} > 0.17$). On the other hand, in the case of bi-dispersed colloidal droplets, $\hat{r}$

remains as a constant during the majority part of the evaporation process (i.e., till $0.75 t_E$ for set A and $0.93\ t_E$ for set B). This suggests that the presence of particles in a droplet promotes the contact line pinning during its evaporation[28]. Accordingly, the contact angle decreases throughout the evaporation process, from a maximum of $27° \pm 1°$ to $7 \pm 2°$ for pure water, as well as for both set A and set B as shown in Fig. 2a.

Fig. 2b presents the morphological pattern of bi-dispersed colloidal droplets of set A (1.0 μm and 6.0 μm particles) and set B (0.2 μm and 3.0 μm particles) with both bright-field and fluorescence microscopy after the evaporation is completed. For set A, only a single ring of smaller (1.0 μm) particles is formed, as shown in the bright-field and fluorescent images, whereas, the larger (6 μm) particles flocculate and form clusters of particles away from the contact line. On the other hand, for set B, two concentric rings are formed, with the smaller particles (0.2 μm) located at the outermost edges and larger particles (3 μm) located inward with a small distance away from the contact line. For both sets of particles, the outward ring is comprised of the smaller particles, 1.0 μm for set A and 0.2 μm for set B. The morphological pattern of the particles under SEM is also shown in Fig. 2b (inset) which displays only a single ring of smaller particles (1 μm) for set A but two concentric rings of particle size 0.2 μm and 3 μm for set B. The distribution of particles in set A and set B was also verified using gray scale intensity plot, as shown in Fig. 2c. For set A, the peak at the right extreme suggests the formation of a single ring due to the smaller particles whereas for set B, presence of two peaks near the contact line suggests formation of two concentric rings due to the 0.2 and 3 μm particles, respectively.

To understand the pinning of the liquid and smaller particles at the contact line, a schematic of an evaporating bi-dispersed colloidal droplet on a hydrophilic substrate and the forces acting on individual particles during evaporation is shown in Fig. 2d. The bi-dispersed colloidal droplet resting on the hydrophilic substrate remains pinned throughout the evaporation process, and the liquid vapour meniscus forms a wedge with the substrate. The evaporation flux across the droplet is not uniform: the evaporation rate is higher at the edge (i.e. three phase contact line) compared to that at the centre of the droplet. To replenish the higher loss of liquid at the contact line due to enhanced evaporation rate, there is a compensated flow from the centre of the droplet toward the three phase contact line. The resulting flow is responsible for driving the particles towards the three-phase contact line. Consequently, the particles of two different sizes get accumulated near the edge of the droplet and form two concentric rings. The smaller particles are located closer to the contact line forming the outer ring, whereas the larger particles are located away from the contact line representing the inner ring, as shown in Fig. 2b and 2d.

In the beginning, in order to replenish the loss of liquid due to enhanced evaporation rate at the edge of the droplet, the particles suspended in the droplet are driven radially towards the contact line due to the outwardly driven capillary flow.
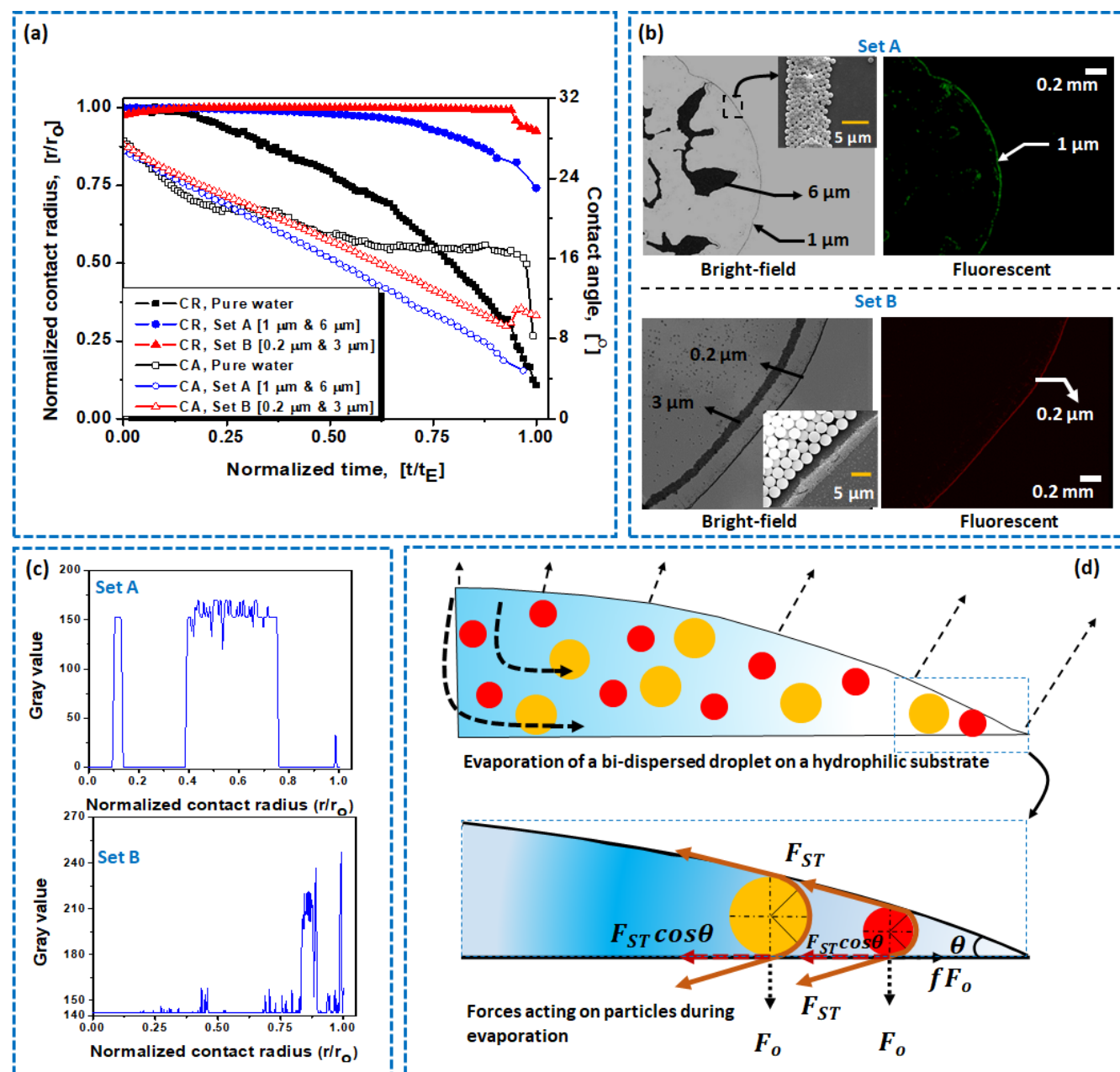

Fig. 2 (a) Variation of normalized contact radius ($\hat{r}$) and contact angle (θ) of bi-dispersed droplets (set A and B) and a DI water droplet (same 1.0 μL volume) on a hydrophilic substrate with time; (b) Morphological pattern of bi-dispersed droplets of set A (1.0 and 6.0 μm particles) and set B (0.2 and 3.0 μm μm particles) after complete evaporation on a hydrophilic substrate under a bright-field and fluorescence microscope; the figures in the inset displaying the morphological pattern under SEM: a single ring of smaller particles (1 μm) for set A but two concentric rings of particle size 0.2 and 3 μm for set B. (c) Gray scale intensity representing the distribution of particles in set A and B on a hydrophilic substrate; (d) Schematic showing an evaporating bi-dispersed droplet on a hydrophilic substrate and the forces acting on the particles during evaporation.

The viscous force is responsible for carrying the particles toward the contact line and the particles are subjected to the drag force[19,29] by

$$F_d = 6\pi r_p \mu v \alpha, \qquad (1)$$

where r_p is the radius of the microparticles, μ is the dynamic viscosity of the fluid, v is the velocity of the evaporative flow and α is the drag coefficient. The various parameters used in the equation above and the equations below and their numerical

values are also given in Table 2 as well. The order of magnitude of the drag force is estimated to be $F_d \sim 10^{-13}$ N.

In addition, the suspended particles inside the droplet are also subjected to the van der Waals and electrostatic interaction forces. The van der Waals force between particles and the substrate in a fluid medium is given by [21,30]

$$F_{vw}^{P-S} = \frac{2A_{PSF}r_p^3}{3z^2(z+2r_p)^2}. \tag{2a}$$

The van der Waals force acting among the particles in a fluid medium is given by

$$F_{vw}^{P-P} = \frac{A_{PSP}r_p}{12z^2}, \tag{2b}$$

where A_{PSF} and A_{PSP} are the Hamaker constant between the polystyrene microparticles and substrate, and between the particles inside the fluid medium, respectively, z is the particle-substrate separation distance. The electrostatic interaction force acting between the particles and the substrate in a fluid medium is given by[31,32]:

$$F_{ER}^{P-S} = -2\pi r_p \epsilon \kappa \frac{[\varphi_1^2 + \varphi_2^2 - 2\varphi_1\varphi_2 \exp(\kappa z)]}{[\exp(2\kappa z)-1]}. \tag{3a}$$

The electrostatic force acting among the particles is given by

$$F_{ER}^{P-P} = -\frac{\epsilon r_p \varphi_1^2}{4} \frac{2\kappa \exp(\kappa z)}{\exp(2\kappa z)+1}, \tag{3b}$$

where ϵ is the water permittivity, κ is the reciprocal of Debye length, φ_1 and φ_2 are the surface potential of the polystyrene microparticles and the substrate respectively. The orders of magnitude of the different forces estimated using equations 1 to 3 are summarized in Table 3.

The positive values of van der Waals force imply an attractive force and the negative values of electrostatic interaction force imply the repulsive force. Since the bond number associated with the droplet is very small, $Bo << 1$, the effect of gravity can be neglected. Thus, with the combination of van der Waals (on the order of $10^{-8}-10^{-9}$ N) and electrostatic interaction force (on the order of $10^{-9}-10^{-10}$ N), the total force acting vertically downward is given by

$$F_o = n(F_{vw}^{P-S} + F_{ER}^{P-S}), \tag{4}$$

where n is the total number of the particle rows[17,33] present at the edge of a droplet. For a pinned droplet, with the evaporation of the bulk liquid, the height or the contact angle decreases though out the evaporation process. As soon as the height of the droplet near the edge reduces to or below the size of the larger particles inside the droplet, a capillary meniscus is

formed, which is sandwiched between two successive particles (see Fig. 2d). Although the height of the liquid meniscus attains a size below the size of the larger particles, the escaping or the protrusion of the particles are not feasible due to the surface tension of the liquid. With the formation of the capillary meniscus, the particles are subjected to the inward surface tension driven force (on the order of 10^{-7} N), which is given by

$$F_{ST} = 2\pi r_p \gamma cos\theta, \tag{5}$$

where γ is the surface tension of the liquid. Consequently, the frictional force induced due to the total vertical force (equation 4) would try to resist the motion. As there are multiple rows present near the contact line, which resist the inward capillary driven motion of the particles, the frictional force is multiplied by 'n' to account for the total vertical force. The surface tension driven force is in competition with the frictional force fF_o, (induced due the total force F_o acting vertically downward, refer Fig. 2d) where f is the frictional coefficient. Among the forces acting, the surface tension force being higher (on the order of 10^{-7} N) in magnitude when compared to the other forces, tends to drag the particles toward the center. However, during the course of evaporation, as more particles accumulate at the edge, more rings are formed, i.e., n in equation 4 increases over time, due to which the frictional force increases and finally balances the surface tension force to give rise to self-pinning (Fig. 2b).

The inward movement of the larger particles (of 6 μm size in set A) and the formation of two concentric rings in set B in our experiments can be explained by using the criteria provided by Sangani et al. [19]

$$\psi \equiv \varphi.Ca.\frac{R^4}{r_p^3 h_o}, \tag{6}$$

where ψ is a dimensionless number used to predict the pinning and depinning of the contact line, φ is the solid fraction, Ca is the capillary number, R is the radius of the contact line, r_p is the radius of the particles, and h_0 is the initial height of the droplet. According to the criterion, whether particles will facilitate the pinning of the contact line or not, depends not only on the particle size but also on the particle volume fraction, droplet radius, evaporation rate, and the wetting characteristics of the substrate. We have calculated the values of ψ for particles of different sizes. For 6 μm particles, the value of ψ was found to be 0.18 , which is smaller than the critical value of $\psi_{crit} = 0.2$ reported by Sangani et al., thus supporting the inward movement of the particles observed in our experiments. For the particles of other sizes, the value of ψ was calculated to be above the critical value, which justifies the pinning of such particles.

Table 2. Details of the various parameters used in equation (1) to (5) and their numerical values.

Parameters	Details	Values
A_{PSF}^{glass}	Hamaker constant between the polystyrene particles and glass, where P denotes the particle, S denotes the substrate, and the F denotes the fluid medium.	3×10^{-20} J[17]
A_{PSF}^{PDMS}	Hamaker constant between the polystyrene particles and PDMS, where P denotes the particle, S denotes the substrate, and the F denotes the fluid medium.	0.1×10^{-20} J[34]
A_{PSP}	Hamaker constant between the particles inside the fluid medium.	0.34×10^{-20} J[35]
z	Particle-substrate separation distance.	0.4 nm[17,21,22,36]
ϵ	Water Permittivity.	7×10^{-10} F/m
κ	Reciprocal of Debye length.	$(430 \times 10^{-9})^{-1}\ m^{-1}$
φ_1	The surface potential of polystyrene microparticles.	-58.89 mV
φ_2^{glass}	Surface potential of the (glass) substrate.	-40 mV[17]
φ_2^{PDMS}	Surface potential of the (PDMS) substrate.	-11.55 mV
μ	Dynamic viscosity of the fluid.	8.90×10^{-4} Pa. s
υ	Velocity of the evaporative flow.	10 μm/s[22]
γ	Surface tension of the liquid-vapour interface.	0.072 N/m
θ	Contact angle of the liquid with the substrate.	27 ± 0.3^o, $110^o \pm 1^o$
f	Frictional coefficient.	0.1[37–39]
r_p	Radius of the particles.	[0.2, 1, 3, and 6] μm
α	Drag coefficient.	1.9[19]

Table 3. Estimation of the orders of magnitude of the different forces on particles in a droplet over a hydrophilic substrate estimated using Equations 1-3.

Force (N)	$d = 1.0\ \mu m$	$d = 6.0\ \mu m$	$d = 0.2\ \mu m$	$d= 3.0\ \mu m$
Drag force, F_d	1.59×10^{-13}	9.54×10^{-13}	3.18×10^{-14}	4.77×10^{-13}
Van der Waals force, F_{vw}^{P-S}	1.57×10^{-8}	9.34×10^{-8}	3.13×10^{-9}	4.67×10^{-8}
Van der Waals force, F_{vw}^{P-P}	8.85×10^{-10}	5.31×10^{-9}	1.77×10^{-10}	2.65×10^{-9}
Electrostatic interaction, F_{ER}^{P-S}	-9.8×10^{-10}	-5.88×10^{-9}	-1.96×10^{-10}	-2.94×10^{-9}
Electrostatic interaction, F_{ER}^{P-P}	-7×10^{-13}	-4.2×10^{-12}	-1.4×10^{-13}	-2.1×10^{-12}
Surface tension, $F_{ST}cos\theta$	2.0×10^{-7}	1.20×10^{-6}	4.0×10^{-8}	6.0×10^{-7}

Hydrophobic substrate

The evaporation kinetics and morphological pattern of bi-dispersed colloidal droplets (set A and B in Table 1) over a hydrophobic (PDMS) substrate are presented in Fig. 3. Fig. 3a depicts the normalized contact radius ($\hat{r} = r/r_o$) and contact angle (θ) against normalized time ($\hat{t} = t/t_E$) of both sets of bi-dispersed colloidal droplets and a DI water droplet during evaporation with the same droplet volume of 1.0 μL. As observed, the droplets are initially pinned for a short period of time ($\hat{t} < 0.33$) during which the normalized contact radius ($\hat{r}$) remains constant and only the contact angle (θ) decreases. When droplet contact angle becomes equal to the receding contact angle of the droplet with the substrate, i.e. $\theta \leq 95.33^o, 99.73^o$ and 93.75^o for set A, set B and pure DI water, the droplet recedes and in that case contact angle remains constant ($0.33 < \hat{t} < 0.80$) while the contact radius decreases.

For $\hat{t} > 0.80\ t_E$ and $\hat{t} > 0.45\ t_E$ for both pure and bi-dispersed colloidal droplets respectively, a mixed mode of evaporation is observed wherein both contact radius and contact angle decrease simultaneously. Similar to the hydrophilic substrate, addition of the particles enhances contact line pinning, thus a droplet with particles remains pinned for a longer duration compared to a pure droplet. Fig. 3b presents the morphological pattern of bi- dispersed colloidal droplets of set A (1.0 and 6.0 μm particles) and set B (0.2 and 3.0 μm μm particles) on a hydrophobic surface after complete evaporation, captured by both bright-field and fluorescence microscopes. Interestingly, the hydrophobic substrate gives rise to a completely different morphological pattern as compared to the hydrophilic substrate. The particles form a centralized deposition pattern with no particles present at the edge (indicated by the dotted line). Fluorescent images (in Fig. 3b) show distribution of smaller (1.0 μm particles in set A and 0.2

μm particles in set B) particles at the edge and the center of the dried droplet. This suggests that for both sets, the particle deposition pattern is similar. It is also observed that smaller particles are found mostly at the center with a small portion of particles at the edge, whereas larger particles are uniformly distributed throughout, as shown in the SEM image in Fig. 4a

and 4b. In order to further quantify the presence of smaller fluorescent particles in both sets, gray scale intensity (for the fluorescently labelled particles) was plotted against the normalized contact radius (r/r_o) as shown in Fig. 3c, which clearly shows higher intensity in the center and the edges, which further supports our claim.
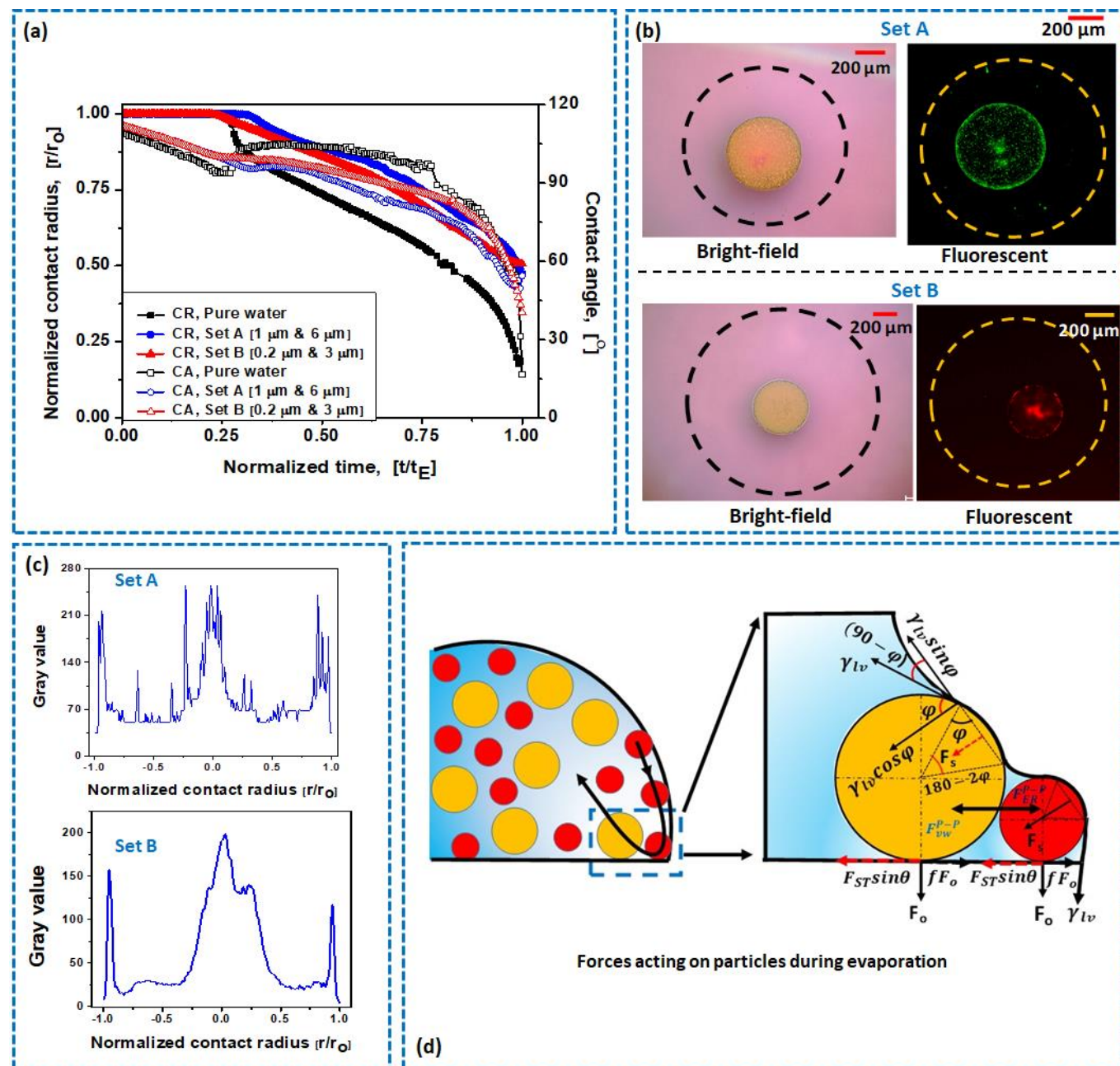

Fig. 3 (a) Variation of normalized contact radius ($\hat{r}$) and contact angle (θ) of both sets of bi-dispersed colloidal droplets and a DI water droplet (1.0 μL volume each) on a hydrophobic substrate with time, (b) Morphological pattern of bi-dispersed colloidal droplets of set A (1.0 and 6.0 μm particles) and set B (0.2 and 3.0 μm μm particles) after evaporation is completed on a hydrophobic substrate, under bright-field and fluorescence microscope, (c) Gray scale intensity representing the distribution of particles in set A and B on a hydrophobic substrate, (d) Schematic showing evaporation of a bi-dispersed colloidal droplet on a hydrophobic substrate and the forces acting on particles during evaporation.

The presence of smaller particles at the center and the edge of the dried droplet on the PDMS substrate can be attributed to

the fact that, a droplet on hydrophobic substrate recedes at the very early stages of evaporation due to the higher receding

contact angle. The droplets on the hydrophobic substrate do not have any singularity in the curvature [40] and the liquid-vapor meniscus does not attain a wedge-like shape. Just prior to receding, particles suspended inside the droplet are under random motion owing to the non-singularity in the curvature of the droplet. During the receding contact line motion ($\hat{t} > 0.33$), the particles are driven inward with the receding contact line till the end of evaporation. The smaller particles experience smaller drag, thus reach the center of the droplet sooner than the larger particles. Towards the end of the evaporation, a mixed mode of evaporation kinetics is observed wherein both contact angle and contact radius decrease simultaneously. In that case, the droplet takes the shape of a liquid wedge and a small fraction of the smaller particles travel radially outward due to the coffee-ring effect and get deposited at the edge of the dried droplet.

Fig. 3d shows a schematic diagram of evaporating particulate droplets over a hydrophobic substrate and various forces acting on the particles. Among the various forces, the van der Waals force is on the order of $10^{-9} - 10^{-10}$ N (Eq 2) among the particles and the particles and substrate. The electrostatic interaction force acting among the particles is on the order of $10^{-12} - 10^{-13}$ N and between the particles and the substrate is on the order of $10^{-8} - 10^{-9}$ N (Eq 3). The viscous drag acting on the particles is on the order of $10^{-13} - 10^{-14}$ N (Eq 1). The surface tension force acting on the particles is given by $F_{ST} = 2\pi r_p \gamma_{lv} cos\varphi$, where $(\pi - 2\varphi)$ is the angle of the liquid layer covering the microparticles[37] as shown in Fig. 3d. The microparticles are pulled inward owing to the horizontal component of the surface tension force, whereas the vertical component of the surface tension contributes to the net vertical force as follows

$$F_o = F_{vw}^{P-S} + F_{ER}^{P-S} + F_{ST} cos\theta. \qquad (7)$$

The net force acting vertically downward is the sum of the van der Waals, electrostatic interaction and the vertical component of the surface tension force. The particles receding toward the center experience the frictional force generated due to the net force acting vertically downward. The self-pinning of the droplet is achieved if the horizontal component of the surface tension force is counterbalanced by the frictional force, as shown below

$$F_{net} = F_{ST} sin\theta - nf F_o. \qquad (8)$$

Similar to the hydrophilic case, the individual forces were estimated for the hydrophobic (PDMS) substrate as presented in Table 4. It is observed that the order of the magnitude of the surface tension force is higher compared to the other forces, thus the particles are driven radially inward and get accumulated at the center of the droplet by forming a centralized deposition pattern. In the present study, we selected different combinations of particles of size ranging from 0.2 to 6 µm to obtain particle size ratios in the range 3 to 30. Both on the hydrophilic (glass) and hydrophobic (PDMS) substrates, the behaviour of particles of size 1 and 3 µm was found to be similar to that of 0.2 and 3 µm whereas the behaviour of particles of size 0.2 and 6 µm was found to be similar to that of 1 and 6 µm (see Fig. 2 and 3). In general, larger particles ($\geq$ 6 µm) would flocculate at the centre and/or sediment whereas smaller particles ($\leq$ 3µm) would not flocculate or agglomerate[41] owing to weaker van der Waals and electrostatic interaction forces (both in terms of particle-particle and particle-substrate interactions) and only form concentric ring patterns. Fig. 4 shows the characterization of the morphological pattern of particles under the SEM and an optical profilometer. The SEM images suggest the presence of both larger and smaller particles at the edge and the center of the droplet as shown in Fig. 4b, whereas, at the intermediate locations, particles of larger size are present as shown in Fig. 4a. Moreover, it is observed that particles are deposited in a closed-packed manner; larger particles at the intermediate locations form hexagonal patterns; while at the edge and center the smaller particles occupy the gaps between the larger particles. Both optical and surface profilometry (Fig. 4c and 4d) characterization indicate a centralized deposition pattern with 90 µm in height.

Table 4. Estimation of the orders of magnitude of different forces acting on the particles in a droplet over a hydrophobic substrate estimated using equations 1 to 3.

| Force (N)	$d = 1.0\ \mu m$	$d = 6.0\ \mu m$	$d = 0.2\ \mu m$	$d = 3.0\ \mu m$
Drag force, F_d	1.59×10^{-13}	9.54×10^{-13}	3.18×10^{-14}	4.77×10^{-13}
van der Waals force, F_{vw}^{P-S}	5.20×10^{-10}	3.11×10^{-9}	1.04×10^{-10}	1.55×10^{-9}
van der Waals force F_{vw}^{P-P}	8.85×10^{-10}	5.31×10^{-9}	1.77×10^{-10}	2.65×10^{-9}
Electrostatic interaction, F_{ER}^{P-S}	-6.15×10^{-9}	-3.69×10^{-8}	-1.23×10^{-9}	-1.85×10^{-8}
Electrostatic interaction, F_{ER}^{P-P}	-7×10^{-13}	-4.2×10^{-12}	-1.4×10^{-13}	-2.1×10^{-12}
Surface tension, $F_{ST} sin\theta$	3.70×10^{-10}	1.85×10^{-9}	5.56×10^{-9}	1.11×10^{-8}

Soft Matter
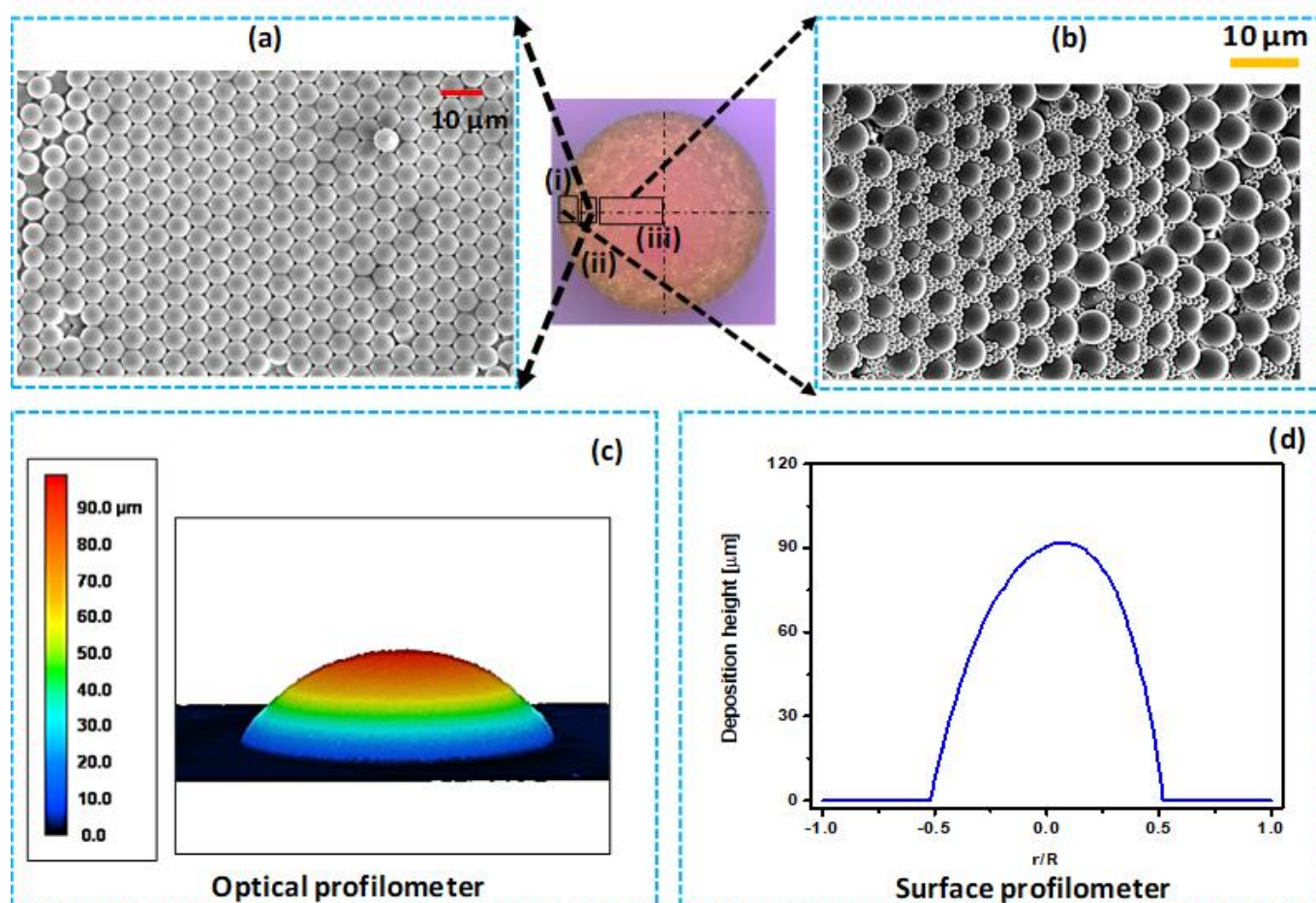
ARTICLE

Fig. 4 (a-b) Morphological pattern of microparticles in set A under SEM showing presence of a mixture of smaller and larger particles at the edge and centre and only larger particles in the intermediate region; (c-d) Shape of the final pattern of microparticles of set A under optical and surface profilometer.

Conclusions

The evaporation kinetics (contact radius and contact angle) and morphological patterns of evaporating bi-dispersed colloidal droplets on hydrophilic ($\theta \sim 27°$) and hydrophobic ($\theta \sim 110°$) surfaces were studied. Our study revealed the formation of a completely different morphological pattern of the micro/nano particles on a hydrophobic substrate ($\theta \sim 110°$) in comparison to those on a hydrophilic surface. On a hydrophobic surface, there was absence of contact line pinning and particles formed a centralized deposition pattern. The order of the magnitude of the surface tension force was found to be higher compared to the frictional force ($\sim 10^{-8}$ N) thus the particles were driven radially inward and get accumulated at the centre of the droplet. Toward the end of droplet evaporation, a mixed mode

of evaporation was observed wherein both contact angle and contact radius decreased simultaneously and a fraction of smaller particles travelled radially outward due to the coffee-ring effect. SEM images confirmed that smaller particles were present mostly at the centre with a small fraction of smaller particles at the edge of the pattern whereas larger particles were uniformly distributed throughout. A phenomenological model that accounts for drag force, van der Waals and electrostatic interaction forces favouring the particle motion and surface tension force opposing the particle motion was employed to illustrate the underlying mechanisms of various morphological patterns. On a hydrophilic surface, depending on the particle size, the surface tension force ($\sim 10^{-7}$ N) was found to be lower or higher than the frictional force arising due to the

van der Waals and electrostatic interaction forces. The smaller particles (0.2 and 1.0 μm), wherein the surface tension force is lower, are found to be pinned and forming an outer ring at the contact line whereas the larger particles (3.0 and 6.0 μm) move inward and either form an inner ring or flocculate, depending on the size.

Conflicts of interest

There are no conflicts to declare.

Acknowledgements

Notes and references

1 Shlomo Magdassi, Amal Bassa, A. Yelena Vinetsky and A. Kamyshny, *Chem. Mater.*, 2003, **15**, 2208–2217.

2 M. Kimura, M. J. Misner, T. Xu, A. Seung Hyun Kim and Thomas P. Russell, *Langmuir*, 2003, **19**, 9910–9913.

3 T. Yoshida, *Prog. Org. Coatings*, 1972, **1**, 73–90.

4 D. Bensimon, A. J. Simon, V. Croquette and A. Bensimon, *Phys. Rev. Lett.*, 1995, **74**, 4754–4757.

5 X. Fang, B. Li, E. Petersen, Y.-S. Seo, V. A. Samuilov, Y. Chen, J. C. Sokolov, A. Chwen-Yang Shew and Miriam H. Rafailovich, *Langmuir*, 2006, **22**, 6308–6312.

6 S. Beaucage, *Curr. Med. Chem.*, 2001, **8**, 1213–1244.

7 M. R. E. Warner, R. V. Craster and O. K. Matar, *J. Colloid Interface Sci.*, 2003, **267**, 92–110.

8 D. B. Williams and C. B. Carter, *The Transmission Electron Microscope: A Textbook for Materials Science*, Springer US, Boston, MA, 2009.

9 P. Dak, A. Ebrahimi, V. Swaminathan, C. Duarte-Guevara, R. Bashir and M. Alam, *Biosensors*, 2016, **6**, 14.

10 H. Y. Erbil, *Adv. Colloid Interface Sci.*, 2012, **170**, 67–86.

11 Hua Hu and R. G. Larson, *J. Phys. Chem. B*, 2002, **106**, 1334–1344.

12 H. Y. Erbil and R. A. Meric, *J. Phys. Chem. B*, 1997, **101**, 6867–6873.

13 R. G. Picknett and R. Bexon, *J. Colloid Interface Sci.*, 1977, **61**, 336–350.

14 A. M. Cazabat, S. Gerdes, M. P. Valignat and S. Villette, *Interface Sci.*, 1997, **5**, 129–139.

15 R. D. Deegan, O. Bakajin, T. F. Dupont, G. Huber, S. R. Nagel and T. A. Witten, *Nature*, 1997, **389**, 827–829.

16 J. Y. Jung and H. Y. Kwak, *Anal. Chem.*, 2007, **79**, 5087–5092.

17 T. S. Wong, T. H. Chen, X. Shen and C. M. Ho, *Anal. Chem*, 2011, **83**, 1871–1873.

18 X. Zhong, H. Xie, and F. Duan, *Appl. Therm. Eng*. **111**, 1565 (2017).

19 A. S. Sangani, C. Lu, K. Su and J. A. Schwarz, *Phys. Rev. E: Stat., Nonlinear, Soft Matter Phys.*, 2009, **80**, 011603 .

20 J. Huang, F. Kim, A. R. Tao, S. Connor and P. Yang, *Nat. Mater.*, 2005, **4**, 896–900.

21 V. H. Chhasatia and Y. Sun, *Soft Matter*, 2011, **7**, 10135.

22 J. Y. Jung, Y. W. Kim, J. Y. Yoo, J. Koo and Y. T. Kang, *Anal. Chem*, 2010, **82**, 784–788.

23 C. C. Monteux and F. O. Lequeux, *Langmuir*, 2011, **27**, 2917–2922.

24 B. M. Weon and J. H. Je, *Phys. Rev. E*, 2010, **82**, 015305(R).

25 J. Y. Jung, W. K. Young and Y. Y. Jung, *Anal. Chem.*, 2009, **81**, 8256–8259.

26 B. M. Weon and J. H. Je, *Phys. Rev. Lett.*, 2013, **110**, 028303.

27 N. R. Devlin, K. Loehr and M. T. Harris, *AIChE J.*, 2016, **62**, 947–955.

28 C. H. Chon, S. Paik, A. Joseph B. Tipton Jr. and K. D. Kihm, *Langmuir*, 2006, **23**, 2953–2960.

29 G. K. Batchelor, *An Introduction to Fluid Dynamics*, Cambridge University Press, Cambridge, 2000.

30 M. (Menachem) Elimelech, *Particle deposition and aggregation : measurement, modelling, and simulation*, Butterworth-Heinemann, 1995.

31 K. Xu, R. Vos, G. Vereecke, G. Doumen, W. Fyen, P. W. Mertens, M. M. Heyns, C. Vinckier and J. Fransaer, *J. Vac. Sci. Technol. B Microelectron. Nanom. Struct.*, 2004, **22**, 2844.

32 R. Hogg, T. W. Healy and D. W. Fuerstenau, *Trans. Faraday Soc.*, 1966, **62**, 1638.

33 W. Li, D. Lan and Y. Wang, *Phys. Rev. E*, 2017, **95**, 042607.

34 J. Visser, *Adv. Colloid Interface Sci.*, 1972, **3**, 331–363.

35 Y. S. Yu, X. L. Xia, X. Zheng, X. Huang and J. Z. Zhou, *Sci. China Physics, Mech. Astron.*, 2017, **60**, 094612.

36 Israelachvili Jacob N, *Intermolecular and Surface Forces*, Elsevier, New York, 3rd edn., 2011.

37 T. Niida, Y. Kousaka and T. Furukawa, *Part. Part. Syst. Charact.*, 1989, **6**, 69–73.

38 N. D. Patil, R. Bhardwaj and A. Sharma, *Langmuir*, 2018, **34**, 12058–12070.

39 B. Bhushan and M. Cichomski, *Cit. J. Vac. Sci. Technol. A*, 2007, **25**, 1285.

40 Y.-S. Yu, M.-C. Wang and X. Huang, *Sci. Rep.*, 2017, **7**, 14118.

41 L. Bansal, P. Seth, B. Murugappan and S. Basu, *Appl. Phys. Lett.*, 2018, **112**, 211605.